Selective hydrogenation of benzene over Ru supported on surface modified TiO$_2$

Fang Hao, Jingsong Zheng, Donghong Ouyang, Wei Xiong[†], Pingle Liu[†], and Hean Luo

College of Chemical Engineering, National & Local United Engineering Research Centre for
Chemical Process Simulation and Intensification, Xiangtan University, Xiangtan 411105, China

Abstract−A series of catalysts with ruthenium nanoparticles (NPs) loaded on the binary oxide TS (TiO$_2$-SiO$_2$) support were prepared by facile sol-gel method for benzene selective hydrogenation. Different mole ratios of Ti/Si were investigated. The catalytic structure, composition, hydrophilicity, electronic state and acidity were characterized. The results indicate that the acidity of the samples increases gradually with the increase of the SiO$_2$ amount. The dispersion of ruthenium nanoparticles was improved on binary oxide support compared with TiO$_2$ and an obvious Ru size effect appeared with the increase of Ti/Si molar ratio. It was also found that the hydrophilicity of the supports could be efficiently improved by introducing a small amount of SiO$_2$ to TiO$_2$, which may be due to the large amount of surface hydroxyl groups on the binary oxide samples after SiO$_2$ introduction. This result was consistent with the increasing trend of cyclohexene yield, indicating that the surface hydroxyl groups play a significant role in the motivation of cyclohexene desorption. Ru/TS (7 : 1) showed the best catalytic performance of 38.2% yield to cyclohexene with the highest initial selectivity to cyclohexene (S$_0$) of 87.3%. The catalytic stability experiments showed that the yield of cyclohexene could maintain at 30% after five cycles.

Keywords: Benzene, Selective Hydrogenation, Ruthenium, TS Binary Oxide, Hydrophilic Modification

INTRODUCTION

The selective hydrogenation of benzene to cyclohexene is an effective alternative process for cyclohexanol synthesis, which is an important intermediate to produce adipic acid or ε-caprolactam (monomers of polyamides) [1,2]. The commercial process for the ε-caprolactam consists of the complete hydrogenation of benzene with 3 mol of hydrogen, and follow-up low efficient cyclohexane oxidation to KA oil (the mixture of cyclohexanone and cyclohexanol), which can only be performed at a low conversion of 4-6% in order to reach high KA oil selectivity. Compared with the drawbacks of relatively low efficiency and expensive feedstock of the cyclohexane oxidation, selective hydrogenation of benzene to produce cyclohexene has been identified to be an attractive alternative route with high atomic utilization and environmentally friendly for the monomers production of polyamides [2].

In terms of thermodynamics point, benzene hydrogenation is more inclined to synthesize complete hydrogenated product cyclohexane with larger standard Gibbs free energy instead of cyclohexene [3-6]. Thus, it remains a great challenge to achieve high cyclohexene selectivity under high conversion of benzene [7-9]. Additionally, selective hydrogenation of benzene involves four-phase reaction systems, including gas phase, oil phase, aqueous phase and solid phase (catalysts). Therefore, an efficient strategy for improving the cyclohexene selectivity should be carried out to promote the desorption of cyclohexene from the catalyst surface as the reaction is proceeding. The design of catalysts with high cyclohexene selectiv-

ity has been the key point in selective hydrogenation of benzene. So far, the noble metal ruthenium has been widely accepted as the most effective active metal for selective hydrogenation of benzene to produce cyclohexene [10,11]. And it has been demonstrated that the supported ruthenium catalyst [12,13] has better catalytic performance compared with that of non-supported ruthenium black catalyst [14,15]. For the support selection, hydrophilic materials such as metal oxide [16-27], molecular sieve [23], hydroxyapatite [28] and polymers [29] are preferred, which is attributed to the water solubility of the target product cyclohexene (23 mol·m^{-3}) being much less than that of benzene (125 mol·m^{-3}). The stable hydrophilic layer generated on the surface of the catalyst is capable of steering the rapid desorption of cyclohexene from the catalyst surface and forming a stagnant layer barrier on the catalyst surface to prevent its re-adsorption, avoiding the deep hydrogenation of cyclohexene to cyclohexane, thus improving the selectivity of cyclohexene [14,18,30-34]. In addition, the yield of cyclohexene can also be markedly improved by introduction of various inorganic additives, e.g., ZnSO$_4$ is commonly used. Literatures have revealed that the role of ZnSO$_4$ in the catalytic system is improving the hydrophilicity of the catalyst by forming a layer of stagnant water on the surface of the catalyst, thereby improving the selectivity of the target product cyclohexene [32,35]. Furthermore, the Zn^{2+} adsorbed on the catalyst surface can also interact with the Ru active site, thus avoiding the deep hydrogenation of cyclohexene to cyclohexane [36].

TiO$_2$ and its composite oxide with strong catalytic ability are widely used in photocatalysis [37-39] and self-cleaning [40,41]. It is indicated that adding a small amount of SiO$_2$ to TiO$_2$ could lead to better performance compared with TiO$_2$ itself. In Yu's work, TiO$_2$/SiO$_2$ composite thin films with addition of 10-20 mol% SiO$_2$ have better hydrophilicity than single TiO$_2$ [42]. Besides, it has been found

[†]To whom correspondence should be addressed.
E-mail: happy.xiongw@163.com, liupingle@xtu.edu.cn

Table 1. The amounts of the materials and the molar ratio of Ti/Si during the preparation

Catalysts	TBOT (g)	TEOS (g)	Ethanol (mL)	Ammonia solution (mL)	Ti/Si[a]
TS (6 : 1)	5.12	0.52	60	2.2	6/1
TS (7 : 1)	5.97	0.61	70	2.6	7/1
TS (8 : 1)	6.83	0.69	80	2.9	8/1
TS (9 : 1)	7.68	0.78	90	3.3	9/1
TiO$_2$	5.12	0	60	1.2	-
SiO$_2$	0	1.04	20	2.0	-

[a]mole ratios of TiO$_2$/SiO$_2$.

that TiO$_2$-SiO$_2$ composite thin films exhibit better thermal stability than TiO$_2$ [43,44]. Based on the superior properties of TiO$_2$-SiO$_2$ composite oxide mentioned above, it is a very promising candidate in selective hydrogenation of benzene to cyclohexene.

Herein, a series catalysts of ruthenium nanoparticles loaded on TS composite oxides with different addition of SiO$_2$ was prepared via sol-gel method and applied to the selective hydrogenation of benzene to produce cyclohexene. The crystal form of TiO$_2$ under different calcination temperature was investigated, the catalytic structure, composition, hydrophilicity and acidity over a series of Ru/TS, Ru/TiO$_2$ and Ru/SiO$_2$ catalysts were characterized and the catalytic performance was tested. It indicated that the introduction of SiO$_2$ could significantly enhance the cyclohexene selectivity, which was identified as the pivotal role of hydrophilicity of the Ru/TS catalyst. Recycle stability of TS (7 : 1) catalyst was also evaluated.

EXPERIMENTAL

1. Materials and Chemicals

RuCl$_3$·3H$_2$O and benzene were purchased from Shanghai Macklin Biochemical Co., Ltd. NaBH$_4$ and aqueous ammonia was supplied from Xilong Chemical Co., Ltd. Tetraethyl orthosilicate (TEOS) were obtained from DaMao chemical Reagent Factory, and tetrabutyl titanate (TBOT) was from Sinopharm Chemical Reagent Co., Ltd. Other chemicals, including Zn(NO$_3$)$_2$·6H$_2$O, ammonia solution (25-28 wt%), were bought from Tianjin kemio Reagent Factory. Ethanol was supplied from Tianjin Guangfu Fine Chemical Research Institute. All used water is deionized water and all reagents were of analytical grade. H$_2$ (99.99%) was provided by Zhuzhou Diamond Gas Company.

2. Catalysts Preparation

The Ru/TS and Ru/TiO$_2$ catalysts were synthesized by two steps. The first step of sol-gel for preparing TS and TiO$_2$ supports and the second step of wetness impregnation-chemical reduction method to fabricate the Ru/TS and Ru/TiO$_2$ at room temperature were carried out in sequence.

Taking preparation of TS (6 : 1) support as an example. Typically, TBOT and TEOS were dissolved to ethanol with ultrasonic dispersion for 5 min and then stirred at room temperature for 10 min. Ammonia solution (25-28 wt%) was then slowly added drop by drop to hydrolyzed TBOT and TEOS, followed by stirring for 2 h. The fabricated white sol was filtered and washed twice with ethanol and deionized water, respectively, and transferred to the oven to dry at 353 K overnight. Finally, the obtained solid as ground

to powder, calcined at 873 K for 2 h to obtain TS (6 : 1) support. TS (7 : 1), TS (8 : 1), TS (9 : 1) supports were also prepared by the same method above with different mole ratios of Ti/Si. The steps for the preparation of TiO$_2$ are the same as that of TS (6 : 1) but no adding TEOS and preparation of SiO$_2$ without adding TBOT. The amount of substances required is shown in Table 1. In addition, the supports of TS (7 : 1) at another calcination temperatures of 773, 973, 1,073, 1,273 K were also prepared for comparing the thermal stability.

Ruthenium loaded catalysts (Ru/TS, Ru/TiO$_2$ and Ru/SiO$_2$) were synthesized by the wetness impregnation-chemical reduction method at room temperature. Taking Ru/TS (6 : 1) for example, specifically, 0.5 g of TS (6 : 1) support was dispersed in 10 mL of deionized water with stirring for 5 min. Next, 3.0 mL of a 0.40 M aqueous solution of RuCl$_3$·3H$_2$O was dropwise added and stirred for 3.5 h. Then 3.0 mL of a 1.58 M aqueous solution of NaBH$_4$ was added dropwise to the slurry under gentle stirring. The ruthenium loading was 8.0 wt% in the catalysts. The molar ratio between NaBH$_4$ and Ru (III) was 4 : 1 to ensure the complete reduction of ruthenium. The black solids were washed thoroughly with deionized water until no chloride ions were detected by the AgNO$_3$ test. Surface analysis also did not identify any residual chlorine on the catalyst. The as-prepared catalysts were denoted as Ru/TS (6 : 1). The other ruthenium supported catalysts prepared with different molar ratios of Ti/Si were marked as Ru/TS (7 : 1), Ru/TS (8 : 1), Ru/TS (9 : 1), Ru/TiO$_2$ and Ru/SiO$_2$, and all these catalysts were evaluated and characterized without additional activation treatment.

3. Catalysts Characterizations

Powder X-ray diffraction (XRD) measurements were taken using a Japan Rigaku D/Max 2550 VB$^+$18 kw X-ray diffract meter with Cu Kα radiation was operating at 40 kV and 30 mA, with a scanning speed of 10 min^{-1} in the range of 2θ=10-90°. Nitrogen adsorption-desorption was performed on an ASAP 2020M automated gas sorption system to measure the specific surface area, pore size distribution and pore volume of the samples. Specific surface area was determined by the method of Brunauer-Emmett-Teller (BET), pore size distribution and pore volume were evaluated from the desorption isotherm branch using the Barrette-Joyner-Halenda (BJH) method. Fourier transform infrared (FT-IR) spectra of the TS, TiO$_2$ and SiO$_2$ supports were performed on a SHIMADZU FTIR-8400s spectrometer in the range of 4,000-400 cm^{-1} with 4 cm^{-1} resolution by signal-averaging 32 scans. Quantitative elemental analysis of active metals Ru was determined by IRIS 1000 Inductively coupled plasma-atomic emission spectroscopy (ICP-AES) (Thermo Elemental, USA).

X-ray photoelectron spectroscopy (XPS) was performed on a Kratos Axis Ultra DLD spectrometer with a monochromatic Al-Kα radiation operating at an invariable transmission energy pass (80 eV). Binding energy (BE) value of different elements in the reference sample was corrected corresponding the peak value of carbon 1s (284.6 eV, accuracy ±0.05 eV). Transmission electron microscopy (TEM), high-resolution TEM (HRTEM), high angle annular dark field-scanning transmission electron microscopy (HAADF-STEM) was carried on a Jem2100 F electron microscope coupled with EDX detector as recorder for elements mapping of the sample. Before characterization, the powder sample was treated by ultrasonic in anhydrous ethanol and then dropped on the copper grid covered with porous carbon film. Surface hydrophilicity of the catalysts was quantified from measurements of the water contact zngle performed on JY-82B equipment. Experiments were performed at room temperature using a goniometer attached to a camera. NH_3-TPD was carried out to measure the amount and strength of surface acid centers of all samples. The samples were heated under Ar for 1 h at 473 K and cooled to 373 K. The mixture gas NH_3/He (10 vol%) at 373 K until the eluted gas chromatographic peak did not change in intensity under thermal conductivity detector (TCD) monitoring. The gaseous and physically adsorbed NH_3 was removed by Ar purge until the signal returned to baseline. The desorption curve of NH_3 was obtained by heating from 373 to 1,073 K at 10 K min^{-1}. The amount of NH_3 adsorbed was calculated according to the area under the desorption curve. CO chemisorption was also performed on the AutoChem II 2920 chemisorption system to test the dispersion of ruthenium nanoparticles. FTIR of adsorbed pyridine (Py-IR) was performed on a Nicolet 470 spectrometer equipped with a temperature-control accessory and a DTGS detector. The sample was pretreated at 473 K for 2 h in a helium atmosphere and then cooled to room temperature and injected with CO pulses until the eluted areas of consecutive pulses became constant. The stoichiometric adsorption of CO was assumed to calculate the amount of ruthenium atoms, and ruthenium surface area was calculated from the ruthenium atomic cross section area.

4. Catalytic Test

The liquid phase hydrogenation of benzene was carried out in a 50 mL Teflon-lined stainless-steel autoclave reactor, which was charged with 0.1 g catalyst, 5 mL benzene, 10 mL deionized water and 1.0 g of $ZnSO_4 \cdot 7H_2O$. After being purged by 0.8 MPa H_2 pressure for five times to remove the air, the reaction was conducted at 423 K and 4.5 MPa H_2 pressure under 1,000 rpm. After the reaction, the autoclave was cooled to room temperature and the reaction product was treated by centrifugation to separate catalyst and collect supernatant for further analysis. The reactant and the product were analyzed by gas chromatography-mass spectrometry (GC-MS, Thermo Fisher Scientific-TXQ Quantum XLS, column-TG-WAXMS, 30 m×0.25 mm×0.25 m), and were quantitatively analyzed by GC (Shimadzu, GC-2010 Plus) equipped with a flame ionization detector FID and a (30 m×0.25 mm×0.25 m) KB-WAX capillary column (Kromat Corporation, USA) using n-hexane as an internal standard. The benzene conversion, products selectivity and yield were calculated by the following equations. Additionally, the catalysts were filtered from the reaction solution and used for

the next run without any other treatment to test the reusability.

$$\text{Benzene conversion} = \frac{\text{moles of benzene consumed}}{\text{initial moles of benzene}} \times 100\% \quad (1)$$

Cyclohexene selectivity

$$= \frac{\text{moles of cyclohexene generated}}{\text{moles of benzene consumed}} \times 100\% \quad (2)$$

$$\text{Cyclohexene yield} = \frac{\text{moles of cyclohexene generated}}{\text{initial moles of benzene}} \times 100\% \quad (3)$$

To compare the intrinsic activity and selectivity of catalysts, the turnover frequency (TOF) was calculated. The TOF calculation formula is as follows [22]:

$$\text{TOF} = \frac{M_{Ru} \times r_0}{W \times \text{dispersion}} \quad (4)$$

M_{Ru} and W are the molar mass of Ru and the loading of Ru on the catalyst, and the Ru dispersion was determined by CO-chemisorption. And r_0 representing the amount of benzene converted per gram of catalyst per minute at zero reaction time was first calculated by the method proposed by Hu et al. [45].

RESULTS AND DISCUSSION

1. Catalytic Structure and Surface Physicochemical Properties

N_2 physisorption isotherms of the samples and their BJH pore size distribution are depicted in Fig. S1. It is indicated that all the samples are mesoporous structure according to the BJH pore size distribution results. It can be observed that the physisorption isotherms of each sample are almost similar, which suggests that the microstructure of the TS sample is preserved after introduction of SiO_2 into TiO_2. The BET surface area, average pore diameter and pore volume of the samples are summarized in Table 2. With the introduction of SiO_2, BET surface area increases with a negligible change of the pore diameter and pore volume.

The XRD patterns of the different samples calcined at 873 K are shown in Fig. 1(A). The diffraction peaks at $2\theta = 25.3°$, $37.8°$, $48.0°$, $53.9°$, $55.1°$, $62.7°$ and $68.8°$ are assigned to the crystal planes of TiO_2 anatase, which indicates that TiO_2 of TS composite oxides exist in the form of anatase. A broad peak around $25°$ in the Ru/SiO_2 and no obvious diffraction peak of SiO_2 in the Ru/TS indicates that SiO_2 is amorphous on the surface of the catalysts. The crystallinity of TS composite oxides increases with increased mole ratio of SiO_2. It also shows that there is no diffraction peak corresponding to the rutile form of TiO_2 in Ru/TS catalysts compared with that of Ru/TiO_2. It can be inferred that the introduction of SiO_2 could inhibit the transformation of anatase to rutile phase of TiO_2, indicating that the SiO_2 introduction could improve the thermal stability of titanium dioxide particles [43,44]. In addition, the XRD patterns of Ru/TS (7 : 1) calcined at different temperature from 773 to 1,273 K are shown in Fig. S2. With the increase of temperature, the crystallinity increased gradually without the generation of rutile phase, which also proved that the introduction of SiO_2 enhanced the thermal stability of TiO_2. Furthermore, there is a weak diffusion peak at ~44°, belonging to the diffraction of hcp-Ru (JCPDS 06-0663) crystal plane, indicating the high dispersion and small

Table 2. Physicochemical properties of Ru/TS and the Ru/TiO₂ catalysts

Catalysts	Ru loading[a] (wt%)	Ru dispersion[b] (%)	BET surface area[c] ($m^2 \cdot g^{-1}$)	Mean pore diameter[c] (nm)	Pore volume[c] ($cm^3 \cdot g^{-1}$)
Ru/TS (6 : 1)	7.9	21.6	17.9	18.7	0.04
Ru/TS (7 : 1)	7.8	24.5	15.3	17.2	0.04
Ru/TS (8 : 1)	7.9	19.6	17.3	17.7	0.03
Ru/TS (9 : 1)	7.2	20.9	14.8	16.9	0.04
Ru/TiO₂	7.5	13.8	11.0	17.4	0.04
Ru/SiO₂	7.6	11.6	51.8	26.2	0.22

[a]Determined by ICP-AES.
[b]Dispersion of Ru determined by CO-chemisorption.
[c]The values were calculated by the BJH method from the adsorption isotherm.
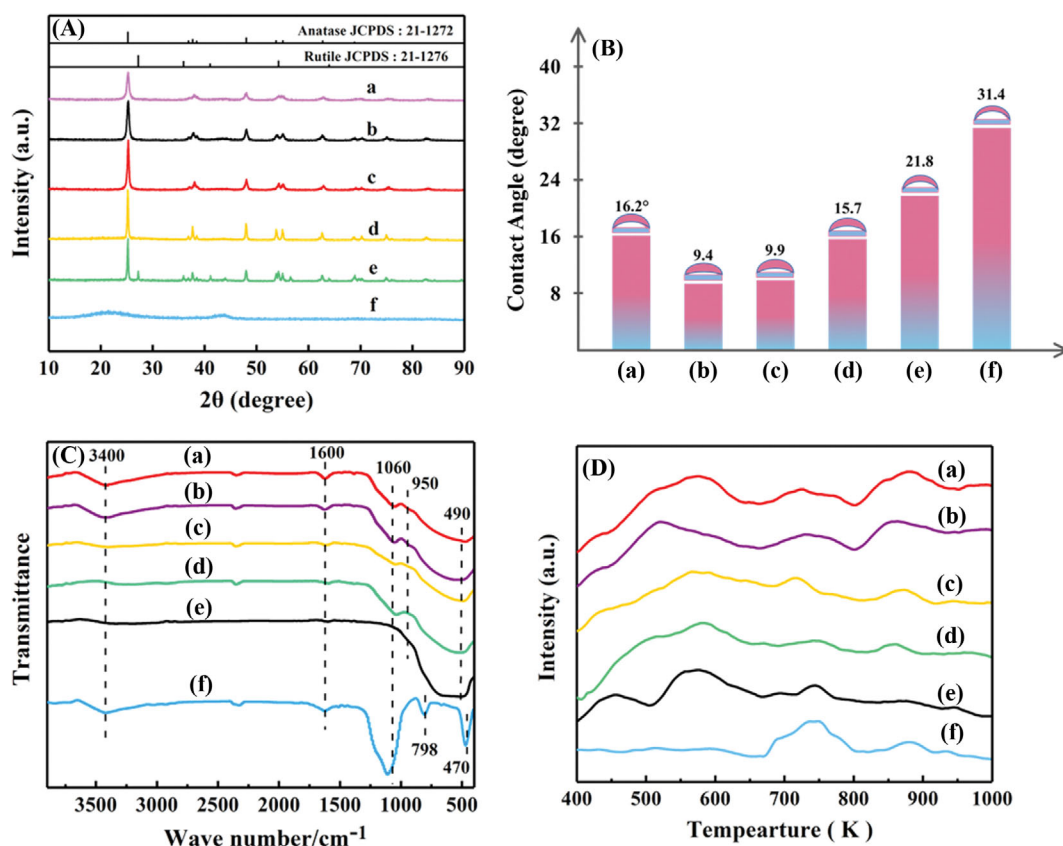
Fig. 1. (A) XRD patterns of Ru/TS (6 : 1) (a), Ru/TS (7 : 1) (b), Ru/TS (8 : 1) (c), Ru/TS (9 : 1) (d), Ru/TiO₂ (e) and Ru/SiO₂ (f); (B) Water contact angles and (C) FT-IR spectra of TS (6 : 1) (a), TS (7 : 1) (b), TS (8 : 1) (c), TS (9 : 1) (d), TiO₂ (e) and SiO₂ (f); (D) NH₃-TPD profiles of the Ru/TS (6 : 1) (a), Ru/TS (7 : 1) (b), Ru/TS (8 : 1) (c), Ru/TS (9 : 1) (d), Ru/TiO₂ (e) and Ru/SiO₂ (f).

size of Ru nanoparticles on the catalyst [46]. The CO chemisorption also proves that the dispersion of ruthenium on Ru/TS is better than that of Ru/TiO₂ and Ru/SiO₂ (Table 2).

The hydrophilicity of the samples was investigated by the method of water contact angles; the results are summarized in Fig. 1(B). TS (7 : 1) with lowest water contact angle (9.4°) shows 22.0% higher hydrophilicity than that of TiO₂, while SiO₂ exhibits the highest angle (31.4°). Besides, it is obvious that all TS samples have better hydrophilicity compared with TiO₂. It may be because TS samples have larger number of surface hydroxyl groups after SiO₂ introduc-

tion, which makes them more hydrophilic. According to Wongkaew [41], adding silica to titanium dioxide increases the acidity of titanium dioxide, and the Ti-O-Si bond of TS interface will lead to more hydroxyl groups on the surface of the film, thus making it more hydrophilic. Another explanation is that the local charge produced at the interface of TS particles is beneficial for the adsorption of dissociated water, which makes the surface of TS support more hydrophilic than TiO₂ [47-50].

The surface hydrophilicity properties of the samples were further verified by FT-IR spectrum. FT-IR spectrum (Fig. 1(C)) shows three

characteristic bands observed at around 1,060 cm⁻¹, 950 cm⁻¹, and 490 cm⁻¹ in all TS samples. The band at around 1,060 cm⁻¹ can be assigned to the stretching of the Si-O-Si bond of the SiO_2 matrixes [51,52]. The band at around 490 cm⁻¹ is the representative of TiO_2 matrixes [53]. While the TS composites exhibit an additional band at around 950 cm⁻¹, which can be assigned to the stretching of the Si-O⁻ species of Si-O-Ti or Si-O defect sites formed by the inclusion of Ti^{4+} ions into the SiO_2 matrixes [54,55]. Thus, the appearance of the band at around 950 cm⁻¹ indicates that the titanium oxide species are embedded into SiO_2 matrixes of the TS composites oxide. Peaks at 798 cm⁻¹ and 470 cm⁻¹ are attributed to the symmetric stretching vibration peaks of Si-O bond. Furthermore, an obvious stretching vibration absorption peak of -OH group located at 1,600 cm⁻¹ and 3,400 cm⁻¹ can be assigned to the bending vibration mode and symmetric stretching vibration of -OH groups of the adsorbed water, respectively, which indicates that the introduction of SiO_2 increases the -OH functional group significantly and makes TS composites oxides much more hydrophilic.

NH₃-TPD curves of different samples are shown in Fig. 1(D). The Ru/TS catalyst has weak, medium and strong acid sites at 572 K, 723 K and 854 K, respectively, while the desorption peak of Ru/TiO₂ does not have a strong acid center at 854 K. The desorption peak of Ru/TS sample at 854 K may be due to the presence of more -OH groups on the surface of SiO_2. Although many literatures have reported that pure silica itself has neither Brönsted acid center nor Lewis acid center, the total amount of acid of Ru/TS catalyst does increase with the introduction of SiO_2, although Ru/SiO₂ shows the lowest acid amount. The amount of NH₃ desorbed by all catalysts presented in Fig. 2. The acidity of Ru/TS catalyst is stronger than that of Ru/TiO₂ and Ru/SiO₂ catalyst. The order of acid sites on the five catalysts is Ru/TS (6:1)>Ru/TS (7:1)>Ru/TS (8:1)≈Ru/TS (9:1)>Ru/TiO₂>Ru/SiO₂.

We further investigated the property and concentration of acid sites of Ru/TS (7:1) and Ru/TiO₂ by Py-IR. Various vibration bands of pyridine at different adsorption sites appeared at 1,446 cm⁻¹ (Lewis acid coordinated pyridine, L-Py), 1,491 cm⁻¹ (ring vibration
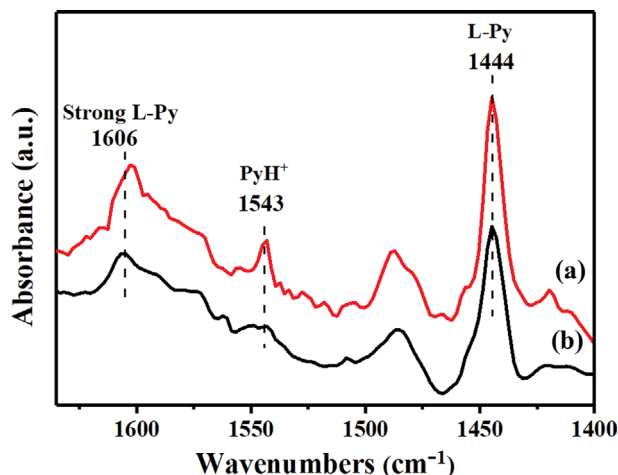
Fig. 3. The Py-IR spectra of the Ru/TS (7:1) (a) and Ru/TiO₂ (b).

of adsorption pyridine), 1,540 cm⁻¹ (Brönsted acid coordinated pyridine, L-py), 1,581 cm⁻¹ (hydrogen-bonded pyridine, hb-Py) and 1,596 cm⁻¹ (strong L-Py) [56-59]. We recorded infrared spectra at 423 K to assess the concentration of the acid center of the samples for the elimination of physically adsorbed pyridine [57]. The Py-IR spectra of Ru/TS (7:1) and Ru/TiO₂ are shown in Fig. 3. For Ru/TiO₂, the characterized peaks at 1,606 and 1,444 cm⁻¹ are assigned to Lewis acid sites and no peaks appeared for Brönsted acid site, while Ru/TS (7:1) shows a characteristic peak at 1,543 cm⁻¹ related to the Brönsted acid site, which indicates that the introduction of SiO_2 could vary the acid sites by generating a large number of OH groups on the catalyst. In addition, the introduction of SiO_2 also increases the intensity of the Lewis acid site shown at 1,606 and 1,444 cm⁻¹, indicating that the introduction of SiO_2 to TiO_2 do increase the acidity of the catalysts, which is in consistent with the results of NH₃-TPD.

2. Microstructure and the Surface Composition of the Samples

The microstructure of supported metal Ru catalysts is further addressed by TEM images shown in Fig. 4(A)-(E). For all Ru/TS catalysts, the size of ruthenium nanoparticles became more uniformly dispersed with the increase of SiO_2 content, which is in good consistence with the results of CO-chemisorption in Table 2. The PSD histogram shows that the mean ruthenium nanoparticles size of 5.1, 5.4, 5.6 and 5.9 nm for the Ru/TS catalysts, all smaller than that of 6.2 nm in Ru/TiO₂, which may result from the reason that doping SiO_2 in TiO_2 can form Ti-O-Si bond and the existence of amorphous SiO_2 around TiO_2 may delay the growth of nanoparticles and reduce their particle size [60]. It has been reported that the dispersion of Ni particles on SiO_2-TiO_2 binary oxides is better than that of TiO_2 due to the interconnection of silica and titanium dioxide [61]. In case of the ruthenium nanoparticle in the present work, it also shows higher dispersion on TS binary oxide supports verified by the results of XRD and TEM. In addition, the HRTEM pictures of Ru/TS (7:1) and Ru/TiO₂ samples in Fig. 4(G), (H) exhibit that the ruthenium nanoparticles are approximately spherical and in close contact with the supports. 0.25 nm is attributed to the crystal plane of TiO_2 anatase {101} lattice and 0.20 nm to the main crystal plane attributed by ruthenium {101} lattice. No lat-
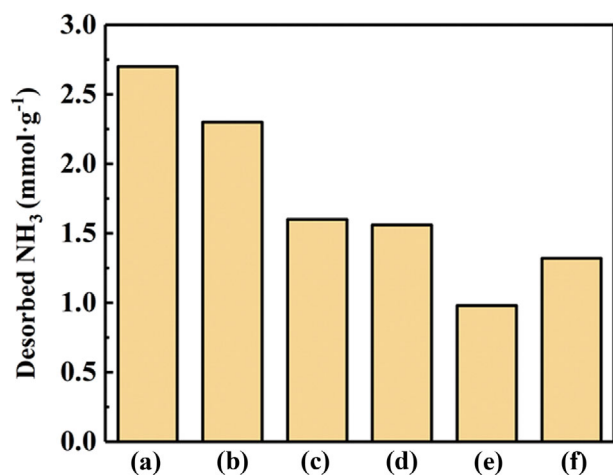

Fig. 2. Total amount of acid sites of Ru/TS (6:1) (a), Ru/TS (7:1) (b), Ru/TS (8:1) (c), Ru/TS (9:1) (d) , Ru/TiO₂ (e) and Ru/SiO₂ (f) determined by NH₃-TPD.

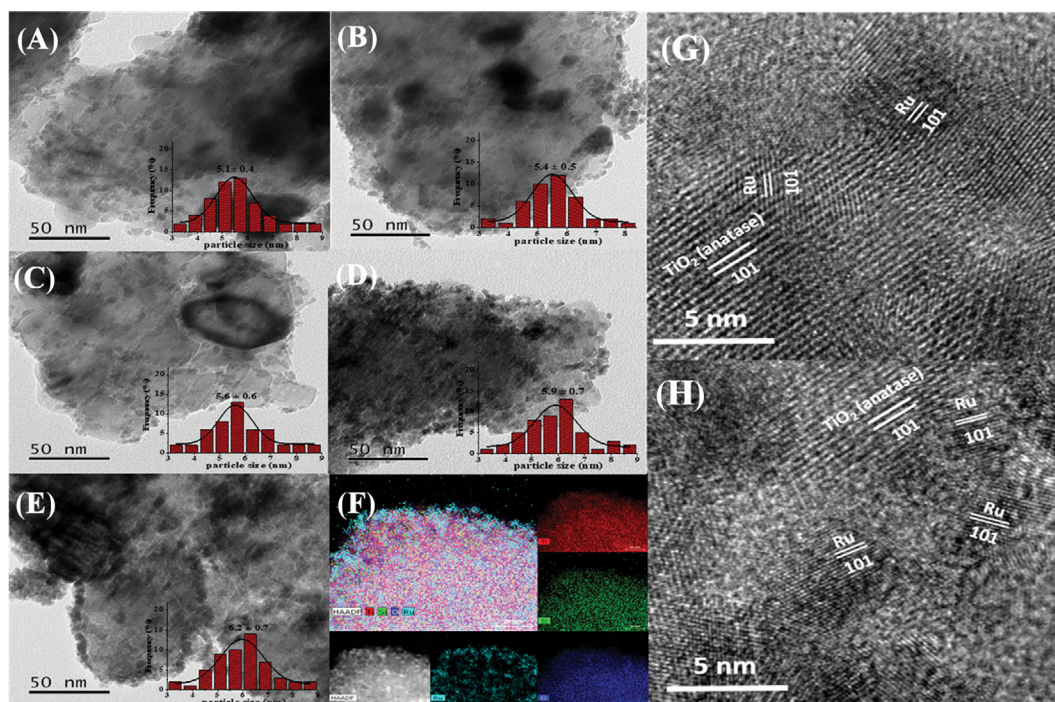Fig. 4. TEM images and the corresponding PSD histograms of the Ru NPs on the Ru/TS (6 : 1) (A), Ru/TS (7 : 1) (B), Ru/TS (8 : 1) (C), Ru/TS (9 : 1) (D) and Ru/TiO₂ (E), EDX mapping and corresponding HAADF-STEM image of the Ru/TS (7 : 1) (F) and HRTEM images of Ru/TS (7 : 1) (G) and Ru/TiO₂ (H).

tice stripes related to silica particles were observed, indicating that the silica phase exists in amorphous form in the catalysts. The distribution of Ru on Ru/TS (7 : 1) is observed by the EDX elemental mapping analysis with corresponding HAADF-STEM image (shown in Fig. 4(F)). It is clear that the Ru NPs were uniformly distributed in the entire region.

Electronic states of the Ru/TS (7 : 1) and Ru/TiO₂ catalysts are examined by XPS spectra and the results of the Ru$3p$ and Ti$2p$ spectra of Ru/TiO₂ and Ru/TS (7 : 1) are presented in Fig. 5. Since the Ti$2p$ peaks partially overlap with the Ru $3p_{3/2}$ peaks, the spectra were deconvoluted to distinguish the respective contributions. The fitting results as for Ru are presented in Table 3. For two catalysts,
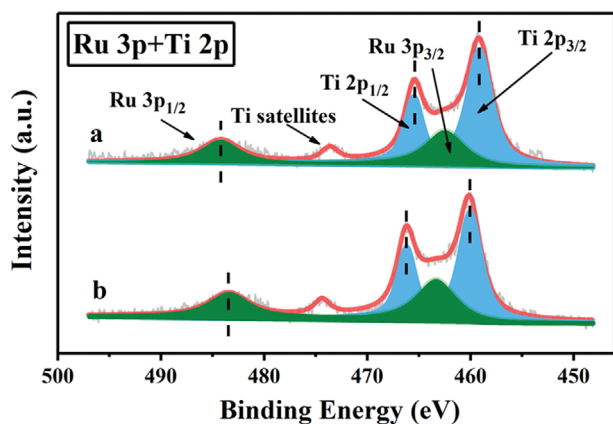
the binding energy of Ru $3p_{1/2}$ and the $3p_{3/2}$-$3p_{1/2}$ doublet separation is in the range of ca. 483.4-484.2 eV and ~22.0 eV, respectively. It indicates that ruthenium elements in Ru/TS (7 : 1) and Ru/TiO₂ exist as metallic Ru [62]. Obviously, binding energy of Ru $3p_{1/2}$ in the two samples is all higher than metal Ru, and a shift for the Ru $3p_{1/2}$ peak from 484.2 eV on the Ru/TiO₂ catalyst to 483.4 eV on the Ru/TS (7 : 1) appeared, signifying that the Ru species on the catalysts are electron-deficient and the electron deficient degree of Ru/TS (7 : 1) is larger than that of Ru/TiO₂, which proved that the introduction of SiO₂ enhances the interaction between metal Ru and the support. Fig. S3 shows the Si$2p$ spectra of Ru/TS (7 : 1) and Ru/TiO₂. With the introduction of SiO₂ appeared the Si-O-Si [63] bond at 102.8 eV, and the peak at 101.9 eV is attributed to the formation of Ti-O-Si bond [63,64], which is consistent with the results of FT-IR (Fig. 1(C)).

3. Selective Hydrogenation of Benzene to Cyclohexene

To compare the intrinsic activity and selectivity of catalysts, the turnover frequency (TOF), weight-specific activity (r_0), and initial

Fig. 5. The Ru$3p$ and Ti$2p$ spectra of the Ru/TS (7 : 1) (a) and Ru/TiO₂ (b).

Table 3. The deconvolution results of the Ru$3p$ spectra of the Ru/TS (7 : 1) and the Ru/TiO₂ catalysts

Catalyst	Peak	Peak position/eV	FWHM/eV[a]
Ru/TS (7 : 1)	Ru⁰ $3p_{1/2}$	484.2	4.48
	Ru⁰ $3p_{3/2}$	462.3	4.43
Ru/TiO₂	Ru⁰ $3p_{1/2}$	483.4	4.51
	Ru⁰ $3p_{3/2}$	462.2	4.54

[a]The full width at half maximum of the peak.

Table 4. Results of the selective hydrogenation of benzene over the Ru/TS and Ru/TiO$_2$ catalysts[a]

Catalyst	t^b (min)	Conv.^{b} (%)	S_{CHE}^b (%)	S_{CHA}^c (%)	Y_{CHE}^b (%)	S_0^d (%)	r_0^e	TOF (s^{-1})
Ru/TS (6 : 1)	15	61.6	44.5	55.5	28.7	76.4	31.9	3.14
Ru/TS (7 : 1)	12	52.4	72.9	27.1	38.2	87.3	34.9	3.07
Ru/TS (8 : 1)	15	62.4	53.5	46.5	33.3	84.1	28.3	3.07
Ru/TS (9 : 1)	15	58.4	51.3	48.7	29.9	76.6	26.8	3.01
Ru/TiO$_2$	15	60.5	43.5	56.5	26.3	69.8	18.1	2.95
Ru/SiO$_2$	16	49.4	39.7	60.3	19.6	59.6	12.7	2.43

[a]Reaction conditions: 0.1 g of catalyst, 5 ml of benzene, 10 ml of H$_2$O, 1.0 g of ZnSO$_4\cdot$7H$_2$O, temperature of 423 K, H$_2$ pressure of 4.5 MPa, and stirring rate of 1,000 rpm.
[b]Values recorded at the maximum yield of cyclohexene.
[c]byproduct cyclohexane selectivity at the maximum yield of cyclohexene.
[d]Initial selectivity towards cyclohexene.
[e]Initial weight specific activity, unit in mmol C$_6$H$_6$ g cat^{-1} min^{-1}.

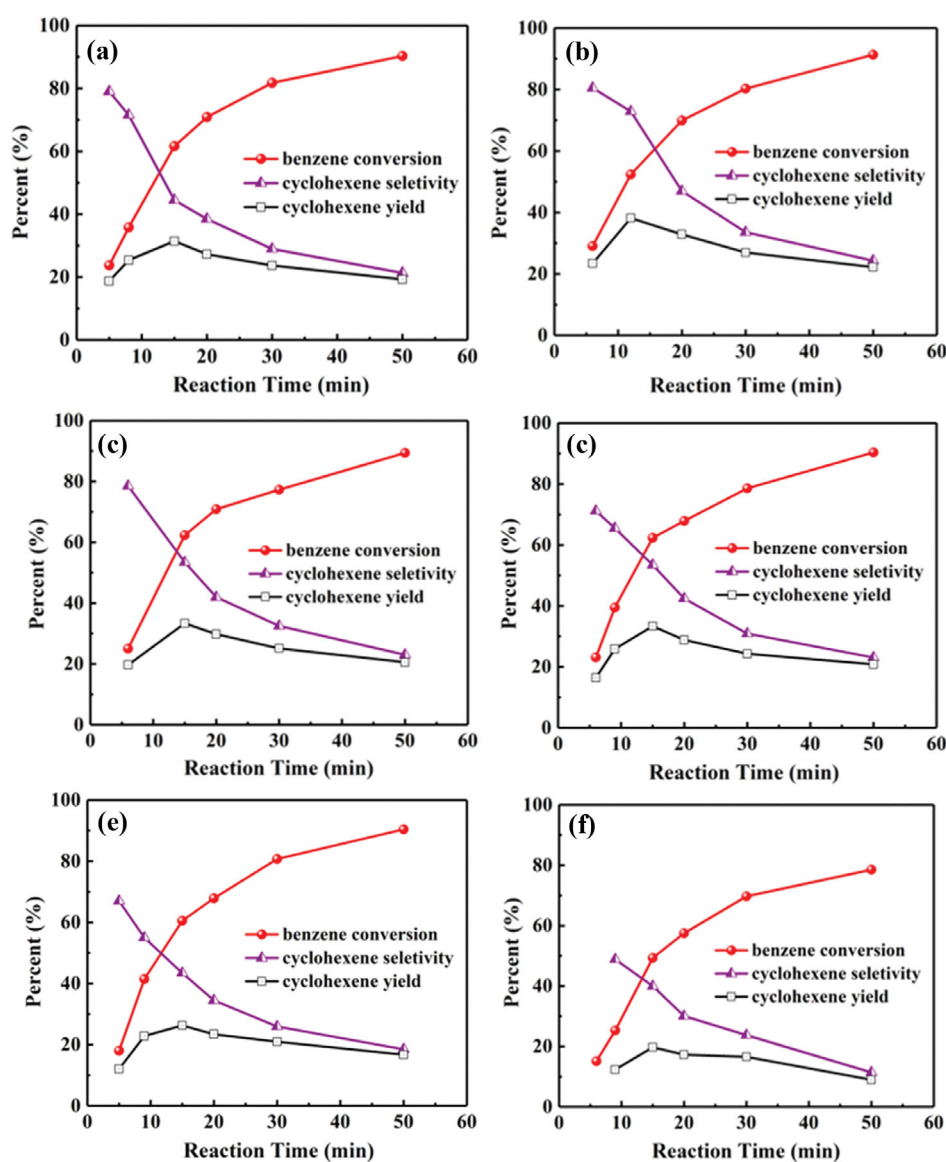
Fig. 6. The benzene hydrogenation over the Ru/TS (6 : 1) (a), Ru/TS (7 : 1) (b), Ru/TS (8 : 1) (c), Ru/TS (9 : 1) (d), Ru/TiO$_2$ (e) and Ru/SiO$_2$ (f) as the reaction progresses. Reaction conditions: 0.1 g of catalyst, 5 ml of benzene, 10 ml of H$_2$O, 1.0 g of ZnSO$_4\cdot$7H$_2$O, temperature of 423 K, H$_2$ pressure of 4.5 MPa, and stirring rate of 1,000 rpm.

selectivity of cyclohexene (S$_0$) were calculated. The correlation curve between the content of benzene and time t was fitted to a polynomial, which was then differentiated over reaction time t, and the intercept obtained by replacing zero with t was r$_0$. Since r$_0$ failed to represent intrinsic hydrogenation activity, the TOFs calculated of benzene for all catalysts were used to analyze. In addition, the linear relationship between selectivity of cyclohexene and reaction time t was fitted, and the curve was extrapolated to zero reaction time (t=0), with the resulting intercept being initial cyclohexene selectivity S$_0$.

Table 4 displays the catalytic results of Ru/TS, Ru/TiO$_2$ and Ru/SiO$_2$ catalysts in selective hydrogenation of benzene. During the reaction, only two products of cyclohexane and cyclohexene were detected under the reaction conditions of 423 K, 4.5 MPa, 1,000 rpm and 1.0 g of ZnSO$_4$·7H$_2$O as additive. As shown in Fig. 6, for all Ru supported samples, the conversion of benzene and the selectivity of cyclohexene exhibit similar variation pattern as reaction proceeding. In the aspect of the curve of cyclohexene yield, there is a semblable volcanic variation tendency for all Ru supported samples. In the whole reaction process, benzene content decreased gradually and cyclohexane content increased monotonically. For cyclohexene, there is a maximum content at a certain period, which is consistent with the known characteristics of continuous hydrogenation. It can be seen in Fig. 6(a)-(e) that among those different TS supported Ru catalysts, the Ru/TS (7 : 1) gives the maximum yield of cyclohexene obtained by Ru/TS (7 : 1) catalyst in 12 minutes, which is 38.2%, among which the benzene conversion is 52.4% with the highest selectivity to cyclohexene (87.3% of initial cyclohexene selectivity), whereas Ru/SiO$_2$ possesses the worst catalytic performance with 19.6% of cyclohexene yield illustrated in Fig. 6(f). It turns out that adding a small amount of SiO$_2$ into TiO$_2$ can indeed improve catalytic performance than Ru/TiO$_2$. In addition, TOFs results showed the same variation tendency as r$_0$. It can been seen that the TOFs increased with the acid amounts of the supports, on account of the additional hydrogenation of benzene on
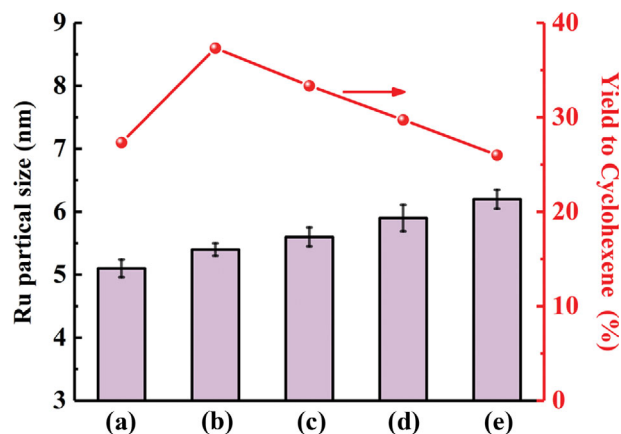

Fig. 7. The correlation of the Ru particle size and the cyclohexene yield on the Ru/TS (6 : 1) (a), Ru/TS (7 : 1) (b), Ru/TS (8 : 1) (c), Ru/TS (9 : 1) (d) and Ru/TiO$_2$ (e).

the acid sites of the support with overflow hydrogen (H$_{so}$) [22,65]. In the case of high hydrogen coverage, Ru/TS catalyst is more likely to spill the dissociated hydrogen onto the support than Ru/TiO$_2$, thus more conducive to the hydrogenation of benzene, which rationalizes the tendency of TOFs.

Fig. 7 shows the variation trend of particle size of Ru and the yield of cyclohexene with the increase of mole ratios of Ti/Si. Note that the yield of cyclohexene exhibited a volcanic-type trend when particle size of Ru increasing from 5.1 nm to 6.2 nm with the increase of Ti/Si, proving that the size of Ru has certain effect on the selective hydrogenation, which can be explained as the variation of hydrophilicity of Ru based catalyst proved by Haijie Sun [66]. It can be also confirmed that the yield of cyclohexene is correlated with the surface hydrophilicity of the support (Fig. 1(B)), on account of more OH groups introduction into TS with the increase of SiO$_2$ depicted in the FT-IR spectra (Fig. 1(C)). Among these catalysts, Ru/TS (7 : 1) has the most amount of OH groups, leading to bet-
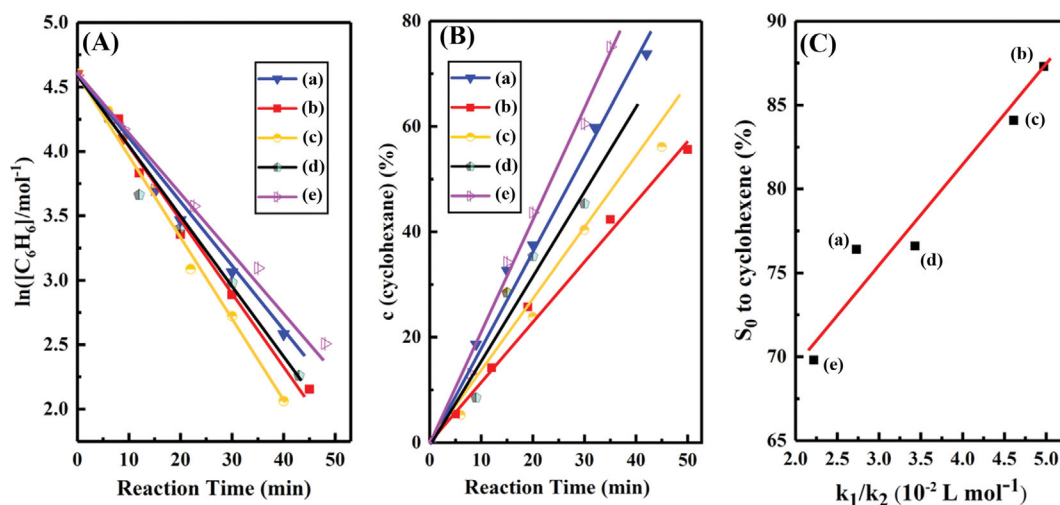

Fig. 8. (A) Plots between the natural logarithm of benzene concentration and reaction time. (B) plots of the cyclohexane concentration with respect to the reaction time and (C) the correlation of k$_1$/k$_2$ with S$_0$ to cyclohexene on Ru/TS (6 : 1) (a), Ru/TS (7 : 1) (b), Ru/TS (8 : 1) (c), Ru/TS (9 : 1) (d) and Ru/TiO$_2$ (e).

ter hydrophilicity and the best catalytic performance was obtained, which is because high hydrophilicity of the catalyst can generate a stable water layer during the reaction process. Furthermore, the solubility of cyclohexene in water is far less than benzene, which led to the timely desorption of generated cyclohexene from the catalyst surface, avoiding the cyclohexene depth hydrogenation to form cyclohexane [14].

From the dynamics point of view, previous studies have shown that the relative hydrogenation rate of benzene to cyclohexene (step 1) is determined to be a first-order reaction, and the relative hydrogenation rate of cyclohexene to cyclohexane (step 2) is determined to be zero-order reaction [13]. By fitting the data obtained from the reaction, steps 1 and 2 are identified as first-order and zero-order reactions, respectively (Fig. 8(A), (B)). According to the slope of the relative dynamics value, two rate constants k_1, k_2 and k_1/k_2 were calculated and listed in Table 5. It can be seen in Fig. 8(C) that the ratio of k_1/k_2 is in accord with the initial selectivity (S_0) to cyclohexene.

4. Optimization of Reaction Parameters

The effect of different H_2 pressure on the catalytic performance of selective hydrogenation of benzene on Ru/TS (7 : 1) was studied (Fig. 9(a)). The selectivity of cyclohexene increased first and then decreased with the increment of H_2 pressure from 3 to 5 MPa. The results show that the selectivity and yield of cyclohexene reached the highest value at 4.5 MPa. It is well known that hydrogenation of benzene is a continuous reaction, and hydrogen pressure has different effects on different steps of benzene hydrogenation. When the hydrogen pressure was lower than 4.5 MPa, different reactants competed for adsorption at the same active site of the catalyst, and the rate of cyclohexene hydrogenation to cyclohexane was lower

than that of benzene hydrogenation to cyclohexene, which justifies that the selectivity of cyclohexene gradually increases with the increase of H_2 pressure [67]. When H_2 pressure was higher than 4.5 MPa, the selectivity of cyclohexene began to decline. This is due to the excess hydrogen covering on the catalyst, which easily accelerates the hydrogenation of cyclohexene to cyclohexane.

Fig. 9(b) exhibits the effect of reaction temperature on the selectivity of cyclohexene over Ru/TS (7 : 1). The yield of cyclohexene increased with the increase of temperature from 403 to 423 K, but further decreased as the temperature continued to rise. The maximum yield of cyclohexene occurred at 423 K. At temperature below 423 K, the surface coverage of hydrogen on the catalyst decreased with the increase of temperature, which is not conducive to the deep hydrogenation of benzene, thus promoting the desorption of cyclohexene from the catalyst surface to obtain higher cyclohexene yield [45]. Above 423 K, the mass transfer rate of cyclohexene from water to the catalyst surface increased and the surface coverage rate of cyclohexene increased continuously, which endows the over-hydrogenation of cyclohexene, thus more likely to reduce the yield of cyclohexene.

In addition, the effect of stirring rate on the selectivity of cyclohexene over Ru/TS (7 : 1) was also investigated (Fig. 9(c)). Cyclohexene selectivity improved gradually with the stirring rate increasing from 600 to 1,000 rpm. This is because the four phases in the reaction system can fully contact and increase the reaction rate under intense stirring rate, which is more conducive to the rapid desorption of cyclohexene from the catalyst surface. As the stirring rate continued to rise to 1,200 rpm, the selectivity of cyclohexene began to decrease significantly. This may be due to the excessive reaction rate, which increases the possibility of contact between cyclo-

Table 5. Catalytic dynamics research on Ru/TS and Ru/TiO$_2$ catalysts

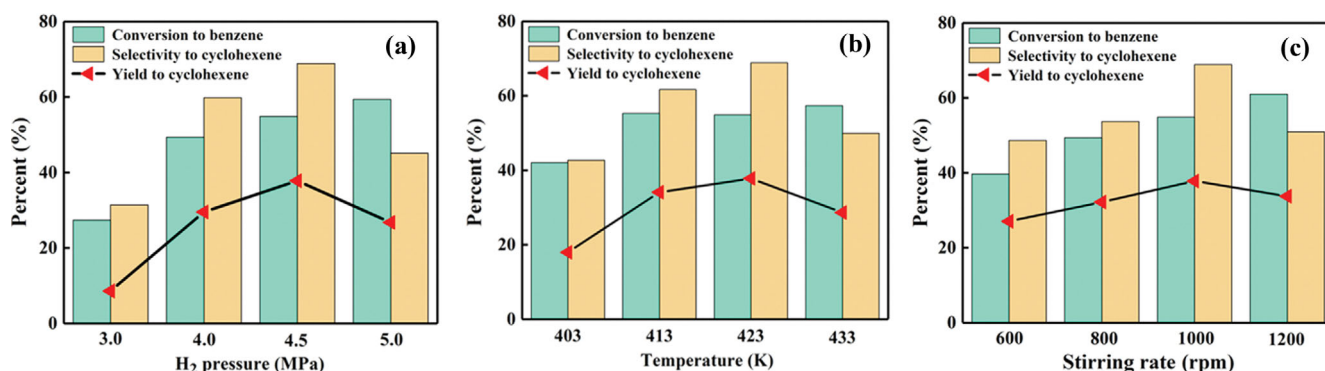| Catalysts	k_1 (10^{-2} min^{-1})	k_2 (10^{-2} L^{-1} min^{-1})	k_1/k_2 (10^{-2} L mol^{-1})
Ru/TS (6 : 1)	4.94	180.8	2.73
Ru/TS (7 : 1)	5.68	114.3	4.97
Ru/TS (8 : 1)	6.27	136.1	4.61
Ru/TS (9 : 1)	5.43	158.1	3.43
Ru/TiO$_2$	4.67	210.5	2.22

Fig. 9. Effects of reaction conditions over Ru/TS (7 : 1) of (a) H_2 pressure, (b) reaction temperature, (c) Stirring rate. Different reaction conditions: (a) Reaction time: 12 min, Reaction temperature: 423 K, Stirring rate: 1,000 rpm; (b) Reaction time: 12 min, H_2 pressure: 4.5 MPa, Stirring rate: 1,000 rpm; (c) Reaction time: 12 min, H_2 pressure: 4.5 MPa, Reaction temperature: 423 K.
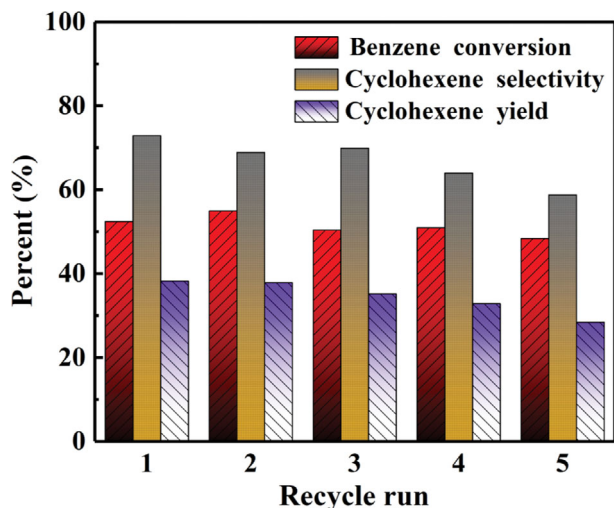
Fig. 10. Reusability of Ru/TS (7 : 1) Reaction conditions: 0.1 g of catalyst, 5 ml of benzene, 10 ml of H$_2$O, 1.0 g of ZnSO$_4$·7H$_2$O, temperature of 423 K, H$_2$ pressure of 4.5 MPa, and stirring rate of 1,000 rpm.

hexene and activated hydrogen, thus causing over-hydrogenation of cyclohexene.

5. Reusability Performance

The recycle stability of the Ru/TS (7 : 1) was investigated under the same reaction conditions and the recycled catalyst did not undergo any additional treatment; the results are shown in Fig. 10. After five catalytic experiments, the conversion of benzene was maintained at 50% and the selectivity of cyclohexene was about 60%. ICP-AES result proves that there is a small amount of leaching of the active component Ru, which was reduced from the original 7.8% to 7.1% after five cycles (Table S1). In addition, as illustrated in Fig. S4, TEM images show that the Ru metal particles on the catalyst were partially agglomerated after five cycles, which also led to the deactivation of the Ru/TS (7 : 1).

CONCLUSIONS

A series of TS supported Ru-based catalysts with different Ti/Si molar ratios were synthesized by sol-gel method. The characterization results show that the dispersion of ruthenium nanoparticles was improved on binary oxide support compared with that on single oxide TiO$_2$, and there was an obvious size effect of ruthenium with the increase of the molar ratio of Ti/Si. Besides, the introduction of SiO$_2$ enhanced the interaction between Ru and the support and could also increase the acidity of the support. Especially, the introduction of SiO$_2$ played a significant role in enhancing the hydrophilicity of TS support by formation of more -OH groups on the catalysts surface than the single TiO$_2$, thus improving the cyclohexene selectivity by promoting its faster desorption. It also indicated that the rate constant k$_1$ of the benzene hydrogenation to cyclohexene was increased and the k$_2$ of the cyclohexene hydrogenation rate to cyclohexane was decreased when the reaction was catalyzed by the Ru/TS. In terms of catalytic performance, the Ru/TS (7 : 1) catalyst shows 38.2% yield to cyclohexene with the larg-

est initial cyclohexene selectivity S$_0$ of 87.3%, and it exhibited good recycle stability in 5 cycles.

SUPPORTING INFORMATION

Additional information as noted in the text. This information is available via the Internet at http://www.springer.com/chemistry/journal/11814.

REFERENCES

1. M. Melgo, A. Lindner and U. Schuchardt, *Appl. Catal. A: Gen.*, **273**, 217 (2004).
2. K. Sato, M. Aoki and R. Noyori, *Science*, **281**, 1646 (1998).
3. N. Bakar, M. Bettahar, M. Bakar, S. Monteverdi and J. Ismail, *J. Mol. Catal. A: Chem.*, **333**, 11 (2010).
4. Y. Li, L. Zhu, K. Yan, J. Zheng, B. Chen and W. Wang, *Chem. Eng. J.*, **226**, 166 (2013).
5. X. Wang, X. Zhang, H. Liu, J. Qiu, W. Han and K. Yeung, *Catal. Today*, **193**, 151 (2012).
6. T. Zhang, X. Zhang, X. Yan, K. Kong, G. Zhang, H. Liu, J. Qiu and K. Yeung, *Chem. Eng. J.*, **228**, 398 (2013).
7. L. Foppa and J. Dupont, *Chem. Soc. Rev.*, **44**, 1886 (2015).
8. F. Schwab, M. Lucas and P. Claus, *Green Chem.*, **15**, 646 (2013).
9. F. Schwab, M. Lucas and P. Claus, *Angew. Chem. Int. Ed.*, **50**, 10453 (2011).
10. C. Fan, Y. Zhu, X. Zhou and Z. Liu, *Catal. Today*, **160**, 234 (2011).
11. Z. Liu, W. Dai, B. Liu and J. Deng, *J. Catal.*, **187**, 253 (1999).
12. D. Rao, X. Xue, G. Cui, S. He, M. Xu, W. Bing, S. Shi and M. Wei, *Catal. Sci. Technol.*, **8**, 236 (2018).
13. X. Xue, J. Liu, D. Rao, S. Xu, W. Bing, B. Wang, S. He and M. Wei, *Catal. Sci. Technol.*, **7**, 650 (2017).
14. X. Yu, Y. Li, S. Xin, P. Yuan and W. Yuan, *Ind. Eng. Chem. Res.*, **57**, 1961 (2018).
15. S. Liu, Z. Liu, Z. Wang, Y. Wu and P. Yuan, *Chem. Eng. J.*, **139**, 157 (2008).
16. L. Jiang and G. Zhou, *J. Catal.*, **382**, 97 (2020).
17. L. Jiang, Y. Dong, G. Zhou, R. Li and D. He, *Ind. Eng. Chem. Res.*, **59**, 1083 (2020).
18. G. Zhou, L. Jiang and D. He, *J. Catal.*, **369**, 352 (2019).
19. G. Zhou, L. Jiang and D. He, *Appl. Catal. A: Gen.*, **575**, 65 (2019).
20. G. Zhou, L. Jiang, Y. Dong, R. Li and D. He, *Appl. Surf. Sci.*, **486**, 187 (2019).
21. T. Wu, P. Zhang, T. Jiang, D. Yang and B. Han, *Sci. China Chem.*, **58**, 93 (2015).
22. G. Zhou, Y. Pei, Z. Jiang, K. Fan, M. Qiao, B. Sun and B. Zong, *J.*

Catal., **311**, 393 (2014).

23. H. Liao, D. Ouyang, J. Zhang, Y. Xiao, P. Liu, F. Hao, K. You and H. Luo, *Chem. Eng. J.*, **243**, 207 (2014).

24. J. Wang, Y. Wang, S. Xie, M. Qiao, H. Li and K. Fan, *Appl. Catal. A: Gen.*, **272**, 29 (2004).

25. C. Milone, G. Neri, A. Donato, M. Musolino and L. Mercadante, *J. Catal.*, **159**, 253 (1996).

26. G. Fan, W. Jiang, J. Wang, R. Li, H. Chen and X. Li, *Catal. Commun.*, **10**, 98 (2008).

27. J. Wang, P. Guo, S. Yan, M. Qiao, H. Li and K. Fan, *J. Mol. Catal. A: Chem.*, **222**, 229 (2004).

28. P. Zhang, T. Wu, T. Jiang, W. Wang, H. Liu, H. Fan, Z. Zhang and B. Han, *Green Chem.*, **15**, 152 (2013).

29. M. Hronec, Z. Cvengrošová, M. Kralik, G. Palma and B. Corain, *J. Mol. Catal. A: Chem.*, **105**, 25 (1996).

30. H. Sun, W. Guo, X. Zhou, Z. Chen, Z. Liu and S. Liu, *Chin. J. Catal.*, **32**, 1 (2011).

31. L. Ronchin and L. Toniolo, *React. Kinet. Catal. Lett.*, **78**, 281 (2003).

32. J. Struijk, M. D'Angremond, W. Regt and J. Scholten, *Appl. Catal. A: Gen.*, **83**, 263 (1992).

33. H. Sun, H. Wang, H. Jiang, S. Li, S. Liu, Z. Liu, X. Yuan and K. Yang, *Appl. Catal. A: Gen.*, **450**, 160 (2013).

34. G. Zhou, X. Tan, Y. Pei, K. Fan, M. Qiao, B. Sun and B. Zong, *ChemCatChem*, **5**, 2425 (2013).

35. S. Xie, M. Qiao, H. Li, W. Wang, J. Deng, *Appl. Catal. A: Gen.*, **176**, 129 (1999).

36. J. Struijk, R. Moene, T. Kamp and J. Scholten, *Appl. Catal. A: Gen.*, **89**, 77 (1992).

37. C. Huang, C. Liao and J. Wu, *Korean J. Chem. Eng.*, **37**, 1352 (2020).

38. M. Eskandarian, M. Rasoulifard, M. Fazli, L. Ghalamchi and H. Choi, *Korean J. Chem. Eng.*, **36**, 965 (2019)

39. H. Jing, J. Huang, N. Li, L. Li and J. Zhang, *Korean J. Chem. Eng.*, **36**, 605 (2019).

40. M. Zhang, E. Lei, R. Zhang and Z. Liu, *Surf. Interface*, **16**, 194 (2019).

41. A. Wongkaew, C. Soontornkallapaki, N. Amhae and W. Lamai, *Adv. Mater. Res.*, **1131**, 237 (2015).

42. J. Yu, X. Zhao, J. Yu, G. Zhong, J. Han and Q. Zhao, *J. Mater. Sci. Lett.*, **20**, 1745 (2011).

43. A. Bedilo, E. Shuvarakova and A. Volodin, *Ceram. Int.*, **45**, 3547 (2019).

44. P. Periyat, K. Baiju, P. Mukundan, P. Pillai and K. Warrier, *Appl. Catal. A: Gen.*, **349**, 13 (2008).

45. S. Hu and Y. Chen, *Ind. Eng. Chem. Res.*, **36**, 5153 (1997).

46. G. Zhou, H. Wang, J. Tian, Y. Pei, K. Fan, M. Qiao, B. Sun and B. Zong, *ChemCatChem*, **10**, 1184 (2018).

47. S. Permpoon, G. Berthomé, B. Baroux, J. Joud and M. Langlet, *J. Mater. Sci.*, **41**, 7650 (2006).

48. M. Houmard, D. Riassetto, F. Roussel, A. Bourgeois, G. Berthome, J. Joud and M. Langlet, *Appl. Surf. Sci.*, **254**, 1405 (2007).

49. M. Houmard, D. Riassetto, F. Roussel, A. Bourgeois, G. Berthome, J. Joud and M. Langlet, *Surf. Sci.*, **602**, 3364 (2008).

50. J. Joud, M. Houmard and G. Berthome, *Appl. Surf. Sci.*, **287**, 37 (2013).

51. F. Ardeshiri, A. Akbari, M. Peyravi and M. Jahanshahi, *Korean J. Chem. Eng.*, **36**, 255 (2019).

52. T. Kim, C. Kim, H. Jeong, C. Shin and Y. Suh, *Korean J. Chem. Eng.*, **37**, 1427 (2020).

53. Y. Zhang, W. Jiang, Y. Ren, B. Wang, Y. Liu, Q. Hua and J. Tang, *Korean J. Chem. Eng.*, **37**, 536 (2020).

54. R. Davis and Z. Liu, *Chem. Mater.*, **9**, 2311 (1997).

55. P. Shao, K. Mauritz and R. Moore, *Chem. Mater.*, **7**, 192 (1995).

56. M. I. Zaki, M. A. Hasan, F. A. Al-Sagheer and L. Pasupulety, *Colloids Surf. A*, **190**, 261 (2001).

57. G. Zhou, Y. Dong and D. He, *Appl. Surf. Sci.*, **456**, 1004 (2018).

58. P. A. Jacobs and C. F. Heylen, *J. Catal.*, **34**, 267 (1974).

59. I. S. Pieta, M. Ishaq, R. P. K. Wells and J. A. Anderson, *Appl. Catal. A: Gen.*, **390**, 127 (2010).

60. H. Zhang and J. Banfield, *J. Mater. Chem.*, **8**, 2073 (1998).

61. M. Lu, Y. Sun, P. Zhang, J. Zhu, M. Li, Y. Shan, J. Shen and C. Song, *Ind. Eng. Chem. Res.*, **58**, 1513 (2019).

62. P. Campbell, C. Santini, F. Bayard, Y. Chauvin, V. Colliere, A. Podgorsek, M. Gomes and J. Sa, *J. Catal.*, **275**, 99 (2010).

63. S. Chenakin, G. Melaet, R. Szukiewicz and N. Kruse, *J. Catal.*, **312**, 1 (2014).

64. S. Ullah, E. Ferreira-Neto, A. Pasa, C. Alcântara, J. Acuna, S. Bilmes, M. Ricci, R. Landers, T. Fermino and U. Rodriguesfilho, *Appl. Catal. B: Environ.*, **179**, 333 (2015).

65. G. Zhou, Y. Dong, L. Jiang, D. He, Y. Yang and X. Zhou, *Catal. Sci. Technol.*, **8**, 1435 (2018).

66. H. Sun, Z. Chen, C. Li, L. Chen, Y. Li, Z. Peng, Z. Liu and S. Liu, *Catalysts*, **8**, 172 (2018).

67. C. Odenbrand and S. Lundin, *J. Chem. Technol. Biotechnol.*, **30**, 677 (1980).